Chinese Chemical Letters 36 (2025) 110495

Contents lists available at ScienceDirect

Chinese Chemical Letters

journal homepage: www.elsevier.com/locate/cclet

High-temperature-stable RRAMs with well-defined thermal effect mechanisms enable by engineering of robust 2D <100>-oriented organic-inorganic hybrid perovskites

Weihong Ding, Kaiyue Song*, Xianglong Li*, Xiaoxia Sun*

Jiangxi Province Key Laboratory of Organic Functional Molecules, Institute of Organic Chemistry, Jiangxi Science and Technology Normal University, Nanchang 330013, China

ARTICLE INFO

Article history:
Received 11 June 2024
Revised 22 September 2024
Accepted 23 September 2024
Available online 24 September 2024

Keywords:
Resistive random-access memory
Organic-inorganic hybrid perovskites
High-temperature resistant
Thermal effect mechanisms

ABSTRACT

The exploitation of organic-inorganic hybrid perovskites (OIHPs) as active layer materials for typical sandwich-structured resistive memories has attracted widespread interest due to the property of low power consumption and fast switching. However, the inherent thermal instability of perovskites limits the application of OIHPs-based resistive memories under extreme conditions, while the influence of thermal effects on their resistance change characteristics remains unclear. Herein, a novel 2D <100>-oriented high-temperature resistant OIHP $[(BIZ\text{-}H)_2(PbBr_4)]_n$ (BIZ = benzimidazole) is prepared as an active layer material to fabricate FTO/$[(BIZ\text{-}H)_2(PbBr_4)]_n$/Ag resistive memory with excellent thermal reproducibility and stability up to 120 °C. The increase in temperature leads to a decrease in the $PbBr_6$ octahedral distortion in the crystal structure, an increase in hydrogen bonding between the $(BIZ\text{-}H)^+$ cation and the $(PbBr_4)_n^{2n-}$ layer, and a shortening of the spacing of the inorganic layers, which is found to result in the creation and predominance of thermally activated traps with increasing temperature. This work provides a new direction for the next generation of OIHPs-based resistive memories with high-temperature tolerance.

Resistive random-access memory (RRAM) is one of the most potential contenders for next-generation memory technologies owing to its structural simplicity, low operating energy efficiency, and fast switching speeds [1-3]. Typically, the structure of an RRAM consists of a bottom electrode/functional layer/top electrode, where the functional layer provides different resistive states, such as low resistance state (LRS) and high resistance state (HRS), which are achieved by voltage amplitude or bias polarity [4]. Various active layer materials have been presented, such as inorganic nitrides/oxides [5], organic small molecules [6], organic polymers [7,8], organic-inorganic hybrid perovskites (OIHPs) [9,10]. However, inorganic materials are hard to process and consume high amounts of power, and organic materials are thermally unstable and environmentally unstable. Generally, OIHPs can exhibit excellent electrical properties by combining the advantages of organic and inorganic materials and compensating for the corresponding disadvantages, which are considered ideal materials for next-generation optoelectronic devices, such as solar cells [11], solar capacitors [12], light-emitting diodes [13], and RRAMs [14]. Currently, OIHPs materials that can be used as RRAMs active layer materials from a structural point of view include 3D and 2D. Among them, 3D OIHPs have been found to react with moisture and air, leading to device degradation, and this degradation further intensifies with increasing temperatures, making them unsuitable for use in special high-temperature environments for data storage such as the aerospace and petroleum industries [4]. In contrast, 2D OIHPs exhibits high stability and hydrophobicity as an active layer material, has low write and erase power consumption, and operates at lower currents with negligible leakage current [15,16]. Unfortunately, the exploitation and detailed mechanism studies of 2D OIHPs-based resistive memories that can be applied to high-temperature environments are very scarce and deserve to be explored in further detail.

From a practical application point of view, the development of resistive variable memories stable at high temperatures for information storage in the aerospace and energy sectors is crucial, as high temperatures can lead to equipment failures [17]. Stable operation of <100>-orientated OIHPs-based resistive memories with molecular formula A_2BX_4 (A is an organic cation and BX_4^{2-} is an inorganic sheet) at high temperatures have been demonstrated, for example, devices based on $(BzA)_2CuBr_4$, BA_2PbI_4 can work at

* Corresponding authors.
E-mail addresses: sky@jxstnu.edu.cn (K. Song), xlli@jxstnu.edu.cn (X. Li), xxsun@jxstnu.edu.cn (X. Sun).

https://doi.org/10.1016/j.cclet.2024.110495
1001-8417/

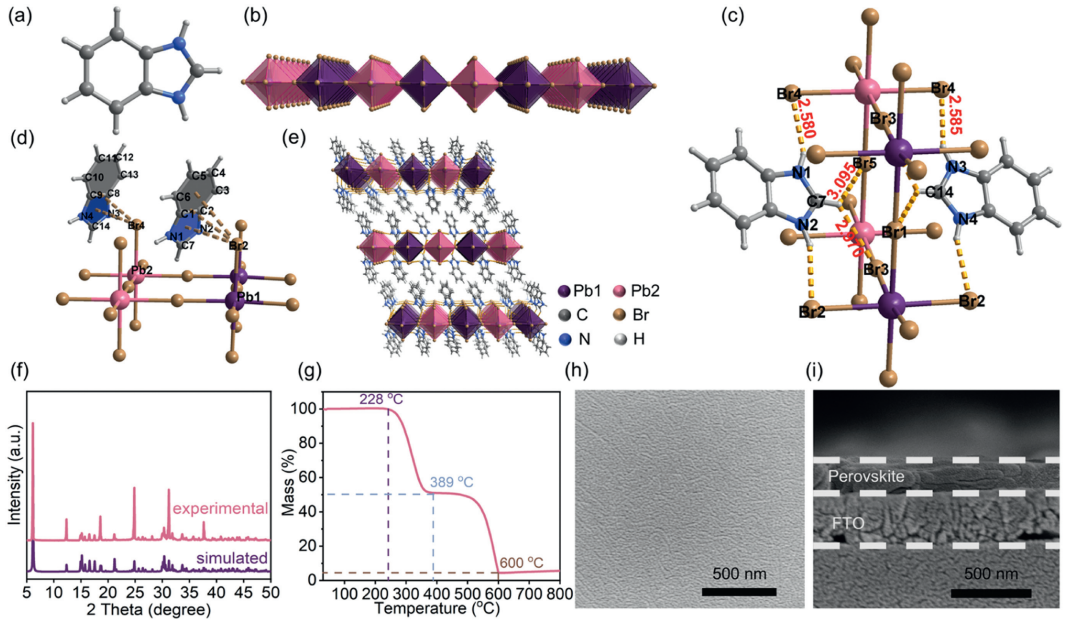

Fig. 1. (a) The structure of $(BIZ\text{-}H)^+$ cation. The grey, blue, and white balls represent C, N, and H atoms, respectively. (b) $(PbBr_4)_n^{2n-}$ layer along the *ac* plane with two crystallographically independent Pb atoms. (c) Hydrogen bondings between $(PbBr_4)_n^{2n-}$ layer and $(BIZ\text{-}H)^+$ cations. Purple, pink, and brown balls represent Pb(1), Pb(2) and Br atoms, respectively. (d) The Pb-Br···π stacking interaction of $[(BIZ\text{-}H)_2(PbBr_4)]_n$. (e) Packing diagram showing the layer-layer distance of $(PbBr_4)_n^{2n-}$. (f) XRD patterns of stimulated, experimental of $[(BIZ\text{-}H)_2(PbBr_4)]_n$. (g) TG curve of the 2D <100>-orientated OIHP $[(BIZ\text{-}H)_2(PbBr_4)]_n$. SEM image of surface (h) and cross-section (i) of the $[(BIZ\text{-}H)_2(PbBr_4)]_n$ film.

85 and 87 °C, respectively [18,19]. The current maximum temperature that <100>-orientated OIHPs-based resistive memory can withstand is 170 °C, but incomplete fracture of the filamentary structure due to Joule heating affects their resistive performance [14]. Therefore, it is vital to explore an OIHP-based resistive memory that is not affected by Joule heating and to elucidate the influence of thermal effects on the resistive behavior of inclusion OIHPs-based resistive memories from the perspective of crystal microstructure.

Herein, we proposed, designed, and prepared a new type of 2D <100>-orientated high-temperature resistant OIHP $[(BIZ\text{-}H)_2(PbBr_4)]_n$ based on benzimidazole (BIZ) with a narrow potential barrier without branched chains, and further as active layer to conducted FTO/$[(BIZ\text{-}H)_2(PbBr_4)]_n$/Ag sandwich device with excellent thermal reproducibility, low energy consumption and stability up to 120 °C. The device has the lowest V_{set} and V_{reset} (0.75, -1.99 V) at 120 °C with a distinguishable HRS/LRS ratio ($>10^2$). In addition, we investigated the crystal structure of $[(BIZ\text{-}H)_2(PbBr_4)]_n$ at room temperature (30 °C) and high temperature (120 °C) using an X-ray single diffraction and by comparison, we noticed that the thermal effects induce a decrease in the $PbBr_6$ octahedral aberration, a shortening of interlayer distances, and an enhancement of the hydrogen bondings, which will inhibit the migration of Br^- or deactivate thermally-activated traps, leading to device resistance change performance failure at higher temperatures. The dominance of thermally activated traps is verified with the aid of *in situ* variable temperature infrared (IR) spectra, UV–vis spectra, and fluorescence spectra. This work provides a new paradigm for RRAMs with high stability in extreme environments.

The novel 2D <100>-orientated OIHP $[(BIZ\text{-}H)_2(PbBr_4)]_n$ was prepared by the reflux method. X-ray single diffraction was used to clarify the structure of $[(BIZ\text{-}H)_2(PbBr_4)]_n$ at room temperature. The conjugated BIZ protonates to the $(BIZ\text{-}H)^+$ cation, with the proton located on the only N atom without an H atom (Fig. 1a). $(PbBr_4)_n^{2n-}$ is a classical planar two-dimensional <100>-oriented inorganic layer constructed from vertex-sharing $PbBr_6$ octahedra along the *bc* plane with two crystallographically independent Pb atoms (Fig. S1 in Supporting information). $(PbBr_4)_n^{2n-}$ layer is close to a planar as viewed from the ac plane (Fig. 1b). The $Pb(1)Br_6$ octahedron constructed by Pb(1) is distorted by the Pb(1)-Br length (2.9744(6)-3.0146(6) Å) and the Br-Pb(1)-Br angle (84.159(10)-95.841(11)°), the $Pb(2)Br_6$ octahedron constructed by Pb(2) is distorted by the Pb(2)-Br length (2.9715(15)-2.9927(6) Å) and Br-Pb(2)-Br angle (83.801(10)-96.199(10)°) (Table S2 in Supporting information). The degree of distortion can be represented by Δd ($\Delta d = (1/6)\sum_{n=1,6}[(d_n\text{-}d)/d]^2$) by Pb-Br lengths and σ^2 ($\sigma^2 = \sum_{n=1,12}(\theta_n\text{-}90°)^2/11$) by Br-Pb-Br angles [20], meanwhile, $\Delta d_{Pb(1)}$ and $\Delta d_{Pb(2)}$ value were calculated as 2.55×10^{-5} and 3.52×10^{-6}, $\sigma^2_{Pb(1)}$ and $\sigma^2_{Pb(2)}$ numerical value were 13.26 and 14.06, implying that the octahedral distortion of $Pb(1)Br_6$ is higher than that of $Pb(2)Br_6$. All hydrogen atoms on the imidazole ring in the $(BIZ\text{-}H)^+$ cation are involved in hydrogen bonding (Fig. 1c and Table S3 in Supporting information). Upon inspection, there is no $\pi\cdots\pi$ stacking action in $[(BIZ\text{-}H)_2(PbBr_4)]_n$. Surprisingly, as shown in Fig. 1d and Table S4 (Supporting information), there are specific Pb-Br···π stacking interactions that act in conjunction with hydrogen bonding to anchor the $(BIZ\text{-}H)^+$ cations in the interlayers, with an interlayer layer-layer perovskite distance of 14.5434(11) Å defined by the nearest Pb···Pb distance (Fig. 1e). The $[(BIZ\text{-}H)_2(PbBr_4)]_n$ crystal structure refinement data are summarized and presented in Table S1 (Supporting information). The experimentally obtained crystal structures were found to remain consistent with the simulated by X-ray diffractometer (XRD) measurements, indicating the successful preparation of 2D <100>-orientated OIHP $[(BIZ\text{-}H)_2(PbBr_4)]_n$ (Fig. 1f). A thermogravimetric (TG) analyzer was employed to characterize the thermal stability of the synthesized 2D <100>-orientated OIHP $[(BIZ\text{-}H)_2(PbBr_4)]_n$, and it was found that the crystalline structure is retained up to 228 °C, and the successive weight loss from 228 °C to 389 °C can be explained by the (BIZ-H)Br decomposition (52.03% calibrated *vs.* 50.08% observed) (Fig. 1g), showing the potential of this crystal to be used as an active layer material for high temperature re-

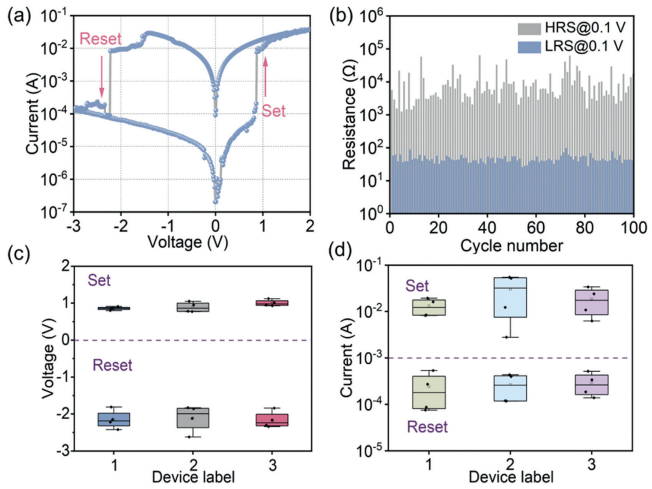

Fig. 2. (a) The *I–V* curves of $[(BIZ\text{-}H)_2(PbBr_4)]_n$-based RRAMs at room temperature. (b) Cycle endurance of 100 rounds. (c) Variation of V_{set} and V_{reset} for the three memory devices. (d) Variation of set current and reset current for the three memory devices.

sistant resistive memory. Hence, we utilize a typical spin-coating method to uniformly coat an organic solution dissolved with $[(BIZ\text{-}H)_2(PbBr_4)]_n$ powder onto the FTO to form a layer-by-layer structure (Fig. S2a in Supporting information). Scanning electron microscopy (SEM) observed that the prepared films were flat and homogeneous (Fig. 1h), meanwhile, both the powder and film patterns closely matched the simulated pattern, indicating the maintenance of the crystalline state on the films (Fig. S3 in Supporting information). The sandwich devices with FTO/$[(BIZ\text{-}H)_2(PbBr_4)]_n$/Ag structure were further prepared with a vertical configuration because of the typical sandwich-structured resistive switching memristor (Fig. S2b in Supporting information) [21]. As shown in Fig. 1i, the thickness of the active layer can be estimated from the cross-sectional SEM image to be about 165 nm. It is worth noting that important previous work has shown that the performance of 2D perovskite-based memristors is independent of the thickness of the active layer material, and therefore, the active layer thickness was not modulated and compared experimentally in this work [22]. These characterizations indicate that 2D <100>-orientated OIHP $[(BIZ\text{-}H)_2(PbBr_4)]_n$ were successfully prepared with high thermal decomposition temperatures, and that sandwich-type resistive memory fabricated with this as the active material is of good quality and are expected to operate in high-temperature environments.

Encouraged by the good thermal stability and the high quality of the sandwich resistive memory, the memristive properties of $[(BIZ\text{-}H)_2(PbBr_4)]_n$ were further examined and characterized. The FTO/$[(BIZ\text{-}H)_2(PbBr_4)]_n$/Ag device was prepared by incorporating an Ag electrode as the top electrode on a layer-by-layer structure based on $[(BIZ\text{-}H)_2(PbBr_4)]_n$ on FTO (Fig. S2 in Supporting information), and the variable-resistance behaviors of FTO/$[(BIZ\text{-}H)_2(PbBr_4)]_n$/Ag device were measured by a typical current-voltage (*I–V*) curve. As shown in Fig. 2a, the *I-V* characteristics of the device at room temperature were obtained after scanning the direct current bias at a fixed position based on -3 V → 0 V → +2 V → 0 V → -3 V with a ramp rate of 0.5 V/s. Typically, the device has bipolar switching characteristics as it can be set at positive bias and reset at negative bias, and the *I-V* curves of FTO/$[(BIZ\text{-}H)_2(PbBr_4)]_n$/Ag device are analyzed in detail: at -3 V → 0 V → +0.80 V, the value of current is small, presenting a high resistance state (HRS) until the voltage reaches approximately +0.80 V, at which point the current suddenly increases and the corresponding voltage is identified as the "set" voltage (V_{set}). At +0.80 V → +2 V → 0 V, the current value increases significantly, presenting a low resistance state (LRS). Subsequently, an opposite "reset" process (V_{reset}) is also observed when the voltage is swept from 0 V to -2.22 V. The average V_{set} and V_{reset} of the ten cycles are 0.92 V and -2.09 V (Fig. S4 in Supporting information). Furthermore, to verify the reproducibility of its resistance-variable storage performance, the device was subjected to 100 rounds of *I-V* cycling, as shown in Fig. 2b, where the resistance window (HRS/LRS ratio) of the device is relatively large at 0.1 V, with the mean HRS and LRS values of 1.06×10^4 and 4.52×10^1 Ω, which is large enough to differentiate between high and low resistance states, showing that the RS behavior of the device has good consistency over 100 consecutive cycles. In addition, to avoid randomness in the resistance-variable storage performance, the switching voltages and currents of the three devices prepared using the same method between the low- and high-resistance states were extracted (Figs. 2c and d), implying that the switching uniformity is reproductive. These results indicate that the 2D <100>-orientated OIHP $[(BIZ\text{-}H)_2(PbBr_4)]_n$ has great potential as an active layer material for non-volatile memory applications.

Exploring high-performance data memory devices in harsh high-temperature environments is very important for specialized industries such as geological exploration, petroleum, steel and chemical production, therefore, the memory performance of the $[(BIZ\text{-}H)_2(PbBr_4)]_n$-based RRAMs at various high temperatures was evaluated [23]. Firstly, the *I-V* curves of the device were determined at 100 °C with the same programmer settings of room temperature. The results show that the average V_{set} and V_{reset} of the device at 100 °C are 0.83 V and -2.06 V (Fig. S5 in Supporting information). Further, the device was subjected to 100 rounds of *I-V* cycling at 100 °C, and the average HRS and LRS values are 8.74×10^3 and 4.89×10^1 Ω, respectively (Fig. S6 in Supporting information), which can still clearly differentiate the high and low resistance states. In attempts to rule out chance in the resistive performance of the devices at 100 °C, the switching voltages and currents of the three same devices were extracted between low- and high-resistance states (Figs. S7 and S8 in Supporting information), which implies that the switching homogeneity is reproducible. These results demonstrated that the FTO/$[(BIZ\text{-}H)_2(PbBr_4)]_n$/Ag device can stably demonstrate the resistive-variable storage performance at 100 °C.

Encouraged by the above outcome, the *I-V* curve of the $[(BIZ\text{-}H)_2(PbBr_4)]_n$-based RRAMs at 120 °C was examined to explore the stability of the resistive-variable performance at higher temperatures. As shown in Fig. 3a, the variable-resistance behavior can be repeated in random 10 cycles at 120 °C. The average V_{set} and V_{reset} of the random ten cycles in *I-V* curves of the $[(BIZ\text{-}H)_2(PbBr_4)]_n$-based RRAMs at 120 °C are 0.75 V and -1.99 V (Fig. 3b). As for the endurance test of the device, the device has withstood 100 turns of *I-V* cycles (Fig. 3c), and the average HRS and LRS values are 9.49×10^3 and 4.91×10^1 Ω, which are still clearly distinguishable between high and low resistance, proving that the device can stably exhibit resistance-variable storage performance under 120 °C. Similarly, the switching voltages and currents of the three devices in the low- and high-resistance states were extracted to exclude chance disturbances (Figs. 3d and e). To further extend the exploration of the resistive storage performance of the device at higher temperatures, the temperature was raised to 150 °C, but unfortunately, the HRS/LRS ratio at 150 °C is so tiny that the high and low resistance states cannot be distinguished, implying that the device fails at 150 °C (Fig. S9 in Supporting information). Hence, a series of tests on *I-V* curves under temperature variation confirms that the $[(BIZ\text{-}H)_2(PbBr_4)]_n$-based RRAMs can withstand a maximum temperature of 120 °C. The resistance storage values at various temperatures are listed in Table 1, and the comparison reveals the lowest V_{set} and V_{reset} at 120 °C (0.75 and 1.99 V). The HRS/LRS ratio at different temperatures is 2.34×10^2 (30 °C), 1.79×10^2 (100 °C), and

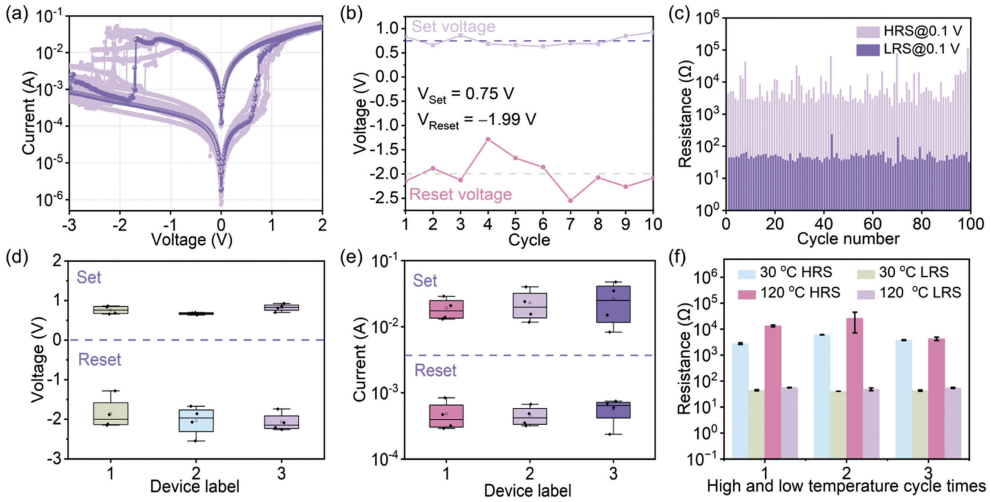

Fig. 3. (a) The *I*–*V* curves of $[(BIZ\text{-}H)_2(PbBr_4)]_n$-based RRAMs at 120 °C. (b) The averaged V_{set}/V_{reset} computed from 10 loops. (c) Cyclic stability testing for 100 rounds. (d) Variation of V_{set} and V_{reset} for the three memory devices. (e) Variation of set current and reset current for the three memory devices. (f) High and low-temperature cycle times.

Table 1
The main resistance changes parameters at 30, 100, 120 °C.

Temperature (°C)	V_{set} (V)	V_{reset} (V)	HRS value (Ω)	LRS value (Ω)	HRS/LRS ratio
30	0.92	-2.09	1.06×10^4	4.52×10^1	2.35×10^2
100	0.83	-2.06	8.74×10^3	4.89×10^1	1.79×10^2
120	0.75	-1.99	9.49×10^3	4.91×10^1	1.93×10^2

1.93×10^2 (120 °C), demonstrating that the resistive-variable storage performance of the device is not significantly degraded even at 120 °C. Subsequently, in consideration of the thermal reproducibility of the $[(BIZ\text{-}H)_2(PbBr_4)]_n$-based RRAMs, the device was raised from 30 °C to 120 °C and then cooled down, and the cycle was repeated three times, and the high and low resistance states maintained (Fig. 3f), indicating that the device possesses a good thermal reproducibility. The performance indicators of the devices at various temperatures are aggregated in Table 1, which indicates that it provides new possibilities for the application of resistive variable memories in high-temperature environments.

The resistive-variable storage performance of OIHPs-based devices can usually be attributed to the formation of conducting filaments due to the migration of halide (iodine or bromine) vacancies [24]. To illustrate the possible carrier transport mechanisms of the FTO/$[(BIZ\text{-}H)_2(PbBr_4)]_n$/Ag resistive-variable memory devices, the *I*-*V* characteristic curves have been redrawn in double logarithmic scale coordinate diagrams (Fig. 4) and the initial state of the device is shown in Fig. 5a. The fitting results imply that when the positive bias voltage in the HRS region is low, the slope of the fitted curve is about 1.12, which follows Ohm's law ($I \propto V$), the injected carriers are dominated by thermal activation, and the injected electrons are trapped in the OIHP layer. $(BIZ\text{-}H)^+$ has a narrow potential barrier and the injected carriers undergo an electron tunneling effect transport into the inorganic layer [22]. As the positive bias voltage increases, the slope of the fitted curve increases to 1.93, which is consistent with the space charge limiting current (SCLC) mechanism, and all traps are gradually filled with injected carriers [25], which generates a reversed inward electric field that prevents the carriers from further injected into the OIHP layer [26], the injected carriers dominate the conduction behavior [27], and the injected carriers grow exponentially, and the current spike results in the transition of the device from the HRS to the LRS, and the slope of the fitted curve is approximately 1.02, which is consistent with Ohm's law (Fig. 4a). Br^- ions migrate along the direction of the electric field, leaving Br^- vacancies in the $(BIZ\text{-}H)^+$ (Fig. 5b) [14]. As the applied voltage increases, Br^- conductive filaments are gradually formed (Fig. 5c). However, during the reverse voltage scan, the device decreases abruptly from LRS to HRS, and the conduction mechanism follows Ohm's law, SCLC, and Ohm's law (Fig. 4b). In reality, this Br^- conductive filament is so thin that it can be easily destroyed by applying a reverse voltage, causing the device to regress from LRS to HRS (Fig. 5d). These mechanistic models have been published in other perovskite-based resistive mem-

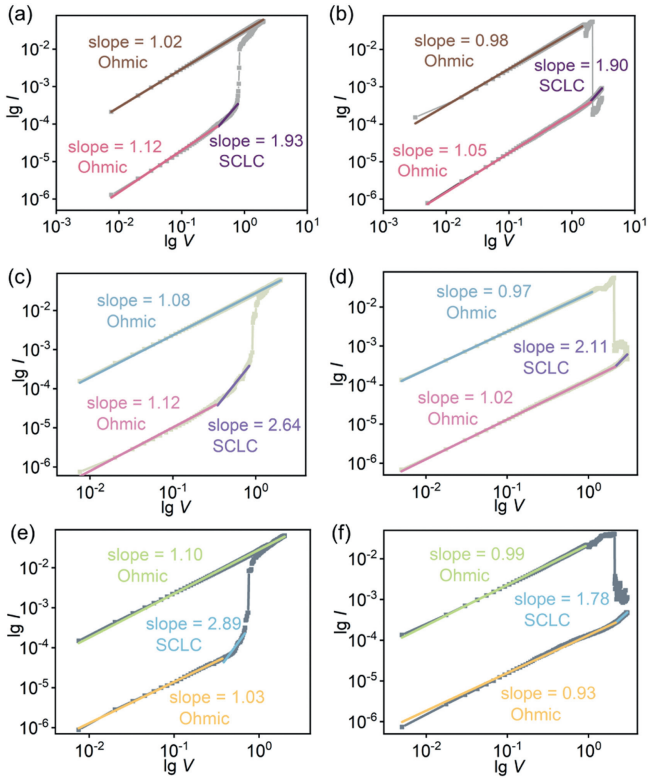

Fig. 4. The lg*I*–lg*V* curves with fitted conduction mechanism under (a) positive- and (b) negative-voltage sweep at 30 °C, (c) positive- and (d) negative-voltage sweep at 100 °C, (e) positive- and (f) negative-voltage sweep at 120 °C.

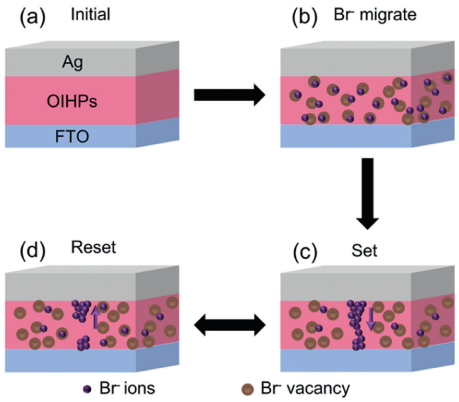

Fig. 5. Mechanism of resistance change in $[(BIZ\text{-}H)_2(PbBr_4)]_n$-based RRAMs at (a) initial state, (b) Br^- migrate, (c) set and (d) reset state.

ories [28,29]. The SCLC slopes at positive voltage increase gradually with increasing temperature, from 1.93 (30 °C) to 2.64 (100 °C, Figs. 4c and d), and 2.89 (120 °C, Figs. 4e and f), which demonstrates that the thermally activated traps are significantly enhanced with increasing temperature. The significant decrease in HRS resistance with increasing temperature confirms that the SCLC process is controlled by the traps [30].

Given further exposing the role of thermal effects on the resistive change storage properties, single-crystal structure analysis, IR, and fluorescence spectra were utilized for exploration. Firstly, to probe the effect of thermal stimulation on the structure of the perovskite, X-ray single diffraction was used to clarify the structure of $[(BIZ\text{-}H)_2(PbBr_4)]_n$ at 30 °C (labeled α-**1**) and 120 °C (labeled β-**1**), focusing on the assessment of the interfacial interactions of $(BIZ\text{-}H)^+/(PbBr_4)_n^{2n-}$ in response to thermal stimulation. After heating to 120 °C, compared to α-**1**, the Pb-Br bond lengths of β-**1** become more uniform and the distortion of the octahedra decreases, with the values of $\Delta d_{Pb(1)}$ and $\Delta d_{Pb(2)}$ decreasing to 1.74×10^{-5} and 2.85×10^{-6}, $\sigma^2{}_{Pb(1)}$ dropping to 13.21, and $\sigma^2{}_{Pb(2)}$ is 14.07 remaining essentially constant (Table S2 in Supporting information). Some of the hydrogen bondings after heating vary little, others become shorter and tend to be strengthened (Fig. 6 and Table S3 in Supporting information), which will inhibit Br^- migration or may deactivate the thermally activated traps, leading to a failure of the resistive change performance of the device at high temperatures. The Pb-Br···π stacking interactions before and after heating are not noticeable modifications (Table S4 in Supporting information), suggesting that they are not responsible for the dominant resistive change properties. The interlayer distance is shortened to 14.4481(20) Å, enhancing Br^- migration and leading to a decrease in V_{set} and V_{reset} with increasing temperature.

Afterward, to further verify the effect of heating on the microcrystalline structure, the temperature-dependent IR and UV–vis spectra were tested, which showed two new absorption peaks after heating for IR spectra (Fig. S10 in Supporting information). One of the peaks at 3755 cm^{-1} is attributed to the N-H bond vibration in the imidazole ring and the other peak at 2347 cm^{-1} can be credited to the resonance of $(BIZ\text{-}H)^+$ [31]. For temperature-dependent UV–vis spectra (Fig. S11a in Supporting information), there are two-dimensional OIHPs characteristic broad excitation absorption bands at 241, 300, 419 and 442 nm [32]. Based on K-M calculations of the UV–vis spectra, a slight tendency for the optical gap to decrease upon heating can be calculated (2.75 eV at 30 °C and 2.74 eV at 120 °C, Fig. S11b in Supporting information), which implies that the interlayer distance becomes shorter [14,33].

Eventually, fluorescence spectra were examined to explore the relationship between heating and traps. From Fig. 7a, it can be seen that the quenching of fluorescence occurs with increasing temperature, which is due to the thermally induced change of the crystalline structure from α-**1** to β-**1** and the appearance of a large number of non-radiative traps, which results in a strong

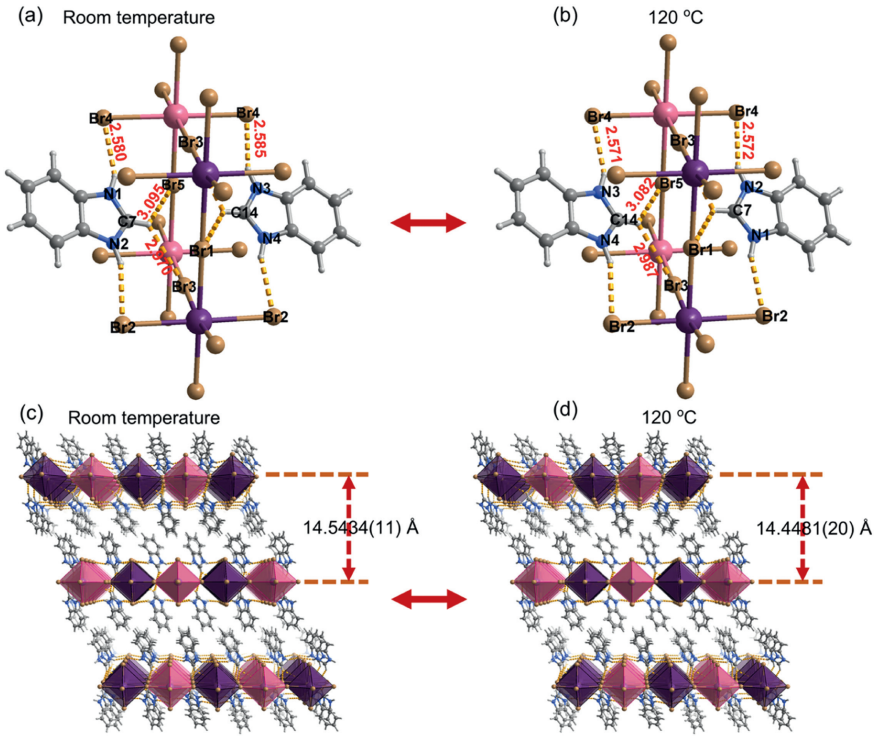

Fig. 6. Hydrogen bondings between $(PbBr_4)_n^{2n-}$ layer and $(BIZ\text{-}H)^+$ cations at (a) 30 °C and (b) 120 °C. $(PbBr_4)_n^{2n-}$ stacking plots of interlayer distances at (c) 30 °C and (d) 120 °C.

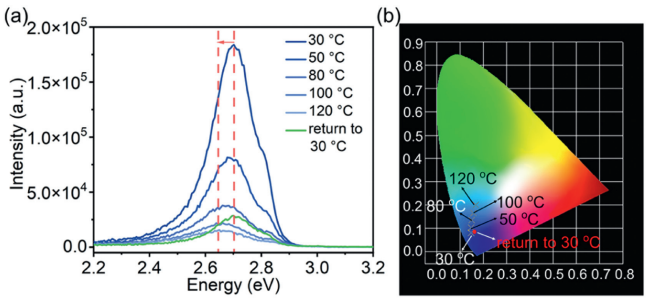

Fig. 7. (a) Fluorescence spectra at various temperatures. (b) CIE-1931 chromaticity chart of $[(BIZ\text{-}H)_2(PbBr_4)]_n$.

thermal quenching. The fluorescence emission peak is red-shifted by 9 nm from 459 nm (2.70 eV, 30 °C) to 468 nm (2.65 eV, 120 °C), which is in line with the trend of optical gap changes derived from K-M calculations of UV–vis spectra and is due to Br^- vacancies in the perovskites with similar activation energies [34]. The fluorescence intensity and peak position show a recovery trend after cooling, which is attributed to the self-elimination of intrinsic defects and non-radiative traps induced by cooling, which suppresses the non-radiative complexation and fluorescence recovery [35]. Thermally-induced fluorescence quenching and recovery can also be seen to be reversible from CIE-1931 chromaticity diagrams and photographs of crystals under UV light (Fig. 7b and Fig. S12 in Supporting information), which confirms the thermal reproducibility of the $[(BIZ\text{-}H)_2(PbBr_4)]_n$-based RRAMs.

In brief, the results from X-ray single-crystal structure analysis, IR, UV–vis, and fluorescence tests at high and low temperatures provide a plausible explanation for the influence of heat on the resistance-varying performance of RRAMs constructed by $[(BIZ\text{-}H)_2(PbBr_4)]_n$-based. The thermally induced enhancement of partial hydrogen bonding, shortening of interlayer distance, reduction of $PbBr_6$ octahedral distortion, smaller optical gap, and fluorescence quenching are favorable to the formation of thermally activated traps, which leads to the better resistive change performance with lower V_{set} and V_{reset} and stable HRS/LRS ratio.

In summary, the novel 2D <100>-type OIHP based on benzimidazole is adopted as an active layer material for the preparation of an FTO/$[(BIZ\text{-}H)_2(PbBr_4)]_n$/Ag resistive-variable memory, and detail explored the temperature dependence of the device and verified its thermally enhanced resistive performance. At room temperature, the rewritable FTO/$[(BIZ\text{-}H)_2(PbBr_4)]_n$/Ag sandwich-like device exhibits promising resistive-variable storage performance, excellent HRS/LRS ratio ($>10^2$), low V_{set} and V_{reset} (0.92 V and -2.09 V), and the $[(BIZ\text{-}H)_2(PbBr_4)]_n$-based resistive-variable memory can be operated at high temperatures of 100, 120 °C maintaining excellent repeatability and stability. More fundamentally, we have investigated the mechanism of the thermally enhanced resistivity of the device from the perspective of the crystal microstructure. As the temperature increases, some hydrogen bonding in the crystal structure is enhanced, the interlayer distance is shortened, the $PbBr_6$ octahedrons distortion is reduced, the optical gap becomes smaller and the fluorescence is quenched, and the thermally activated traps dominate, and the device exhibits lower V_{set} and V_{reset} as well as significantly differentiated HRS/LRS ratios. These results provide new opportunities for the development of novel perovskite-based resistive memories that operate under extreme conditions.

Declaration of competing interest

The authors declare that they have no known competing financial interests or personal relationships that could have appeared to influence the work reported in this paper.

CRediT authorship contribution statement

Weihong Ding: Writing – original draft, Investigation, Conceptualization. **Kaiyue Song:** Writing – review & editing, Supervision, Funding acquisition. **Xianglong Li:** Writing – review & editing, Funding acquisition. **Xiaoxia Sun:** Writing – review & editing, Supervision, Resources.

Acknowledgments

This work was financially supported by the Ph.D. start-up funds of Jiangxi Science and Technology Normal University (Nos. 2023BSQD11, 2023BSQD13), and Jiangxi Province Key Laboratory of Organic Functional Molecules (No. 2024SSY05141).

Supplementary materials

Supplementary material associated with this article can be found, in the online version, at doi:10.1016/j.cclet.2024.110495.

References

[1] J.J. Yang, M.D. Pickett, X. Li, et al., Nat. Nanotechnol. 3 (2008) 429–433.
[2] D.B. Strukov, G.S. Snider, D.R. Stewart, et al., Nature 453 (2008) 80–83.
[3] R. Waser, M. Aono, Nat. Mater. 6 (2007) 833–840.
[4] S. Lee, H. Kim, D.H. Kim, et al., ACS Appl. Mater. Interfaces 12 (2020) 17039–17045.
[5] J.L. Feng, W. Hu, F.J. Zeng, et al., Appl. Phys. Lett. 117 (2020) 192012.
[6] H. Cao, Q.J. Zhang, H. Li, et al., J. Mater. Chem. C 9 (2021) 569–574.
[7] K.Y. Song, H.L. Yang, B.J. Chen, et al., Appl. Surf. Sci. 608 (2023) 155161.
[8] K.J. Zhao, J.X. Liu, X.Z. Wang, et al., Adv. Opt. Mater. 12 (2024) 2301761.
[9] K.Y. Song, P.K. Zhou, L.L. Zong, et al., Chin. Chem. Lett. 34 (2023) 107464.
[10] K.Y. Song, L.L. Du, G.L. Yue, et al., J. Colloid Interface Sci. 642 (2023) 408–420.
[11] E.L. Unger, E.T. Hoke, C.D. Bailie, et al., Energy Environ. Sci. 7 (2014) 3690–3698.
[12] J. Liang, G.Y. Zhu, C.X. Wang, et al., Nano Energy 52 (2018) 239–245.
[13] J.W. Lee, Y.J. Choi, J.M. Yang, et al., ACS Nano 11 (2017) 3311–3319.
[14] K.Y. Song, B.J. Chen, X.L. Lin, et al., Adv. Electron. Mater. 8 (2022) 2200537.
[15] Y.L. Sun, L. Qian, D. Xie, et al., Adv. Funct. Mater. 29 (2019) 1902538.
[16] M. Kumar, H.S. Kim, D.Y. Park, et al., ACS Appl. Mater. Interfaces 10 (2018) 12768–12772.
[17] S. Gao, X.H. Yi, J. Shang, et al., Chem. Soc. Rev. 48 (2019) 1531–1565.
[18] S.Y. Kim, J.M. Yang, E.S. Choi, et al., Adv. Funct. Mater. 30 (2020) 2002653.
[19] J.Y. Seo, J. Choi, H.S. Kim, et al., Nanoscale 9 (2017) 15278–15285.
[20] X.T. Sun, H.F. Ni, Y. Zhang, et al., Chin. J. Struct. Chem. 6 (2023) 100212.
[21] K.J. Kwak, D.E. Lee, S.J. Kim, et al., J. Phys. Chem. Lett. 12 (2021) 8999–9010.
[22] J. Ghosh, S. Parveen, P.J. Sellin, et al., Adv. Mater. Technol. 8 (2023) 2300400.
[23] F.M. Ma, Y.B. Zhu, Z.W. Xu, et al., Adv. Funct. Mater. 30 (2020) 1908901.
[24] H.J. Jeong, C. Park, H. Jeon, et al., ACS Appl. Mater. Interfaces 13 (2021) 40891–40900.
[25] Y.M. Yuan, Y.C. Wang, X.S. Tang, et al., ACS Appl. Mater. Interfaces 14 (2022) 53990–53998.
[26] X.F. Cheng, X. Hou, J. Zhou, et al., Small 14 (2018) 1703667.
[27] X.H Zhang, X.N. Zhao, X.Y. Shan, et al., ACS Appl. Mater. Interfaces 13 (2021) 28555–28563.
[28] S.P. Ge, X.W. Guan, Y.T. Wang, et al., Adv. Funct. Mater. 30 (2020) 2002110.
[29] X.J. Zhu, J.H. Lee, W.D. Lu, Adv. Mater. 29 (2017) 1700527.
[30] J. Zhou, W. Li, Y. Chen, et al., Adv. Mater. 33 (2021) 2006201.
[31] D. Yerezhep, Z. Omarova, A. Aldiyarov, et al., Molecules 28 (2023) 1288.
[32] E.R. Dohner, A. Jaffe, L.R. Bradshaw, et al., J. Am. Chem. Soc. 136 (2014) 13154–13157.
[33] S.H. He, S.Q. Hao, J.W. Lin, et al., Inorg. Chem. 61 (2022) 11973–11980.
[34] C. Eames, J.M. Frost, P.R.F. Barnes, et al., Nat. Commun. 6 (2015) 7497.
[35] J.X. Zheng, G.C. Yue, Z.A. Zhou, et al., Adv. Funct. Mater. 33 (2023) 2300607.